JPE 16-1-31

http://dx.doi.org/10.6113/JPE.2016.16.1.297
ISSN(Print): 1598-2092 / ISSN(Online): 2093-4718

# Stationary Frame Current Control Evaluations for Three-Phase Grid-Connected Inverters with PVR-based Active Damped LCL Filters

Yang Han†, Pan Shen*, and Josep M. Guerrero**

†,*Department of Power Electronics, School of Mechatronics Engineering, University of Electronic Science and Technology of China (UESTC), Chengdu, China
**Department of Energy Technology, Aalborg University, Aalborg, Denmark

## Abstract

Grid-connected inverters (GCIs) with an LCL output filter have the ability of attenuating high-frequency (HF) switching ripples. However, by using only grid-current control, the system is prone to resonances if it is not properly damped, and the current distortion is amplified significantly under highly distorted grid conditions. This paper proposes a synchronous reference frame equivalent proportional-integral (SRF-EPI) controller in the $\alpha\beta$ stationary frame using the parallel virtual resistance-based active damping (PVR-AD) strategy for grid-interfaced distributed generation (DG) systems to suppress LCL resonance. Although both a proportional-resonant (PR) controller in the $\alpha\beta$ stationary frame and a PI controller in the $dq$ synchronous frame achieve zero steady-state error, the amplitude- and phase-frequency characteristics differ greatly from each other except for the reference tracking at the fundamental frequency. Therefore, an accurate SRF-EPI controller in the $\alpha\beta$ stationary frame is established to achieve precise tracking accuracy. Moreover, the robustness, the harmonic rejection capability, and the influence of the control delay are investigated by the Nyquist stability criterion when the PVR-based AD method is adopted. Furthermore, grid voltage feed-forward and multiple PR controllers are integrated into the current loop to mitigate the current distortion introduced by the grid background distortion. In addition, the parameters design guidelines are presented to show the effectiveness of the proposed strategy. Finally, simulation and experimental results are provided to validate the feasibility of the proposed control approach.

**Key words:** Active damping, LCL filter, PVR-AD scheme, Stability, Synchronous frame equivalent PI

## I. INTRODUCTION

Recently, distributed generation (DG) systems based on renewable energy systems, such as photovoltaics and wind turbines, have been attracting more and more attention. These renewable energy sources are usually installed in a distributed way. The grid-connected inverter (GCI), as an interface between DGs and the network, plays an important role in ensuring that high-quality power is injected to the grid [1]-[4].

In a GCI, an *L* filter or an *LCL* filter is usually used as an interface between the inverter and the grid. However, if only an inductor is used, high-frequency (HF) switching is needed to ensure that no excessive switching ripples are generated from the pulse-width modulation (PWM) process, which is accompanied by the undesirable problems of excessive switching losses and electromagnetic interference (EMI), especially in high-power applications [5]. Compared to the classical *L* filter, the *LCL* filter has better attenuation capacity of the switching harmonics and better dynamic characteristics, which usually results in a lower volume and cost [6]. However, the *LCL* filter is a three-order system and instability problems may occur at the resonant frequency, thus proper damping solutions are mandatory to stabilize the whole system [7].

The ways to damp resonance problems can be classified into passive damping (PD) and active damping (AD) methods.

Manuscript received Apr. 29, 2015; accepted Jul. 24, 2015
Recommended for publication by Associate Editor Kyo-Beum Lee.
†Corresponding Author: hanyang_facts@hotmail.com
Tel: +86-13730606846, Fax: +86-28-6183-0229, UESTC
*Dept. of Power Electronics, School of Mechatronics Eng., University of Electronic Science and Technology of China (UESTC), China
**Dept. of Energy Technology, Aalborg University, Denmark

PD is achieved by inserting an additional resistor in series or in parallel with the filter inductor or filter capacitor [8]. The PD scheme of adding a resistor in series with the filter capacitor has been widely adopted due to its simplicity and high reliability. However, the additional resistor will result in power loss and decrease the attenuation of the LCL filter [9]. In order to overcome these drawbacks, the concept of a virtual resistor was proposed. This concept is called the AD method [10], [11]. An interesting control strategy based on the feedback of the splitting capacitor current was proposed in [12]. With this method, the injected current is not controlled directly, and the damping capability relies on the LCL parameters. Therefore, among the AD methods, the methods involving the feedback of the capacitor current have attracted a considerable amount attention due to their simple implementation and wide applicability [2], [13]-[17].

Another interesting approach, which is the main focus of this paper, is to consider the current controller implementation so that better performance is ensured. It is well-known that the proportional integral (PI) controller has an infinite gain for the dc component. This guarantees precise tracking of the dc references without steady-state errors. However, for ac references, a PI controller leads to steady-state errors due to the finite gain at the selected frequency [18], [19]. Proportional resonant (PR) controllers can provide an infinite gain at the selected resonant frequency to suppress the effects of unwanted harmonics, which ensures zero steady-state errors when tracking an ac reference at the selected frequency [20]-[22]. On the other hand, applying a PI controller in the *dq* synchronous frame can ensure zero steady-state errors, since the ac signal is transformed into a dc signal, which insures that an infinite gain is achieved by the PI controller at the dc component [23], [24]. However, the synchronous frame PI control scheme requires accurate phase synchronization of the grid voltage by using a phase-locked-loop (PLL), which may deteriorate the tracking performance under grid disturbances [24]. Moreover, the straightforward analysis method, referred to as the PI model, replace the PI controller in the *dq* synchronous frame with a PI plus resonant controller in the *αβ* stationary frame. However, the approximation is not accurate and the coupling terms are ignored [25]. In [26], an accurate synchronous frame equivalent PI (SRF-EPI) in the stationary frame with an *L* filter was presented. This method shows robust performance under a wide frequency range. However, systems with *LCL* resonance are not considered and the effects of power-stage parameter deviations and grid background distortion were not taken into account. In addition, the discrete model and the control delay effect were also neglected.

This paper proposes a novel parallel virtual resistance (PVR)-based AD method integrated with the SRF-EPI control strategy in the *αβ* stationary frame for three-phase grid-connected inverters with an LCL filter. Multiple PR controllers and a grid voltage feed-forward loop for improving tracking precision under background grid distortion conditions are investigated when the proposed strategy is used. Moreover, the SRF-EPI, PI and PR controllers are analyzed, designed and compared to show the feasibility and effectiveness of the proposed strategy.

This paper is organized as follows. In Section II, the system description and the proposed control scheme are presented. The damping characteristics of the various PD schemes, the series virtual resistance (SVR) and PVR-based AD strategies are analyzed, and the use of the SRF-EPI, PI and PR controllers are compared in the stationary frame. Section III presents parameter design guidelines. The impact of LCL-parameter variations based on the SRF-EPI controller in the stationary frame is also studied. Section IV presents simulation and experimental results of a 2.2 kVA three-phase DG system. Finally, Section V concludes this paper.

## II. System Description and Control Scheme

Fig. 1 shows the topology of a three-phase grid-connected voltage source inverter (VSI) based on an LCL filter, where the inductor parasitic resistances are neglected. In addition, a switch is used to choose the current controllers, and $G_{PI}(s)$, $G_{eq}(s)$, and $G_{PR}(s)$ correspond to the PI controller, the SRF-EPI controller, and the PR controller, respectively. To achieve a good filtering performance, the resonance frequency of the LCL filter should be in the range of $10f_0<f_{res}<(f_s/2)$, where $f_0$ denotes the fundamental frequency, $f_{res}$ represents the resonance frequency, and $f_s$ is the switching frequency [7], [18], [27]. Based on these guidelines, the parameters of the power-stage are given in Table I.

### *A. Stationary Frame SRF-EPI, PI, and PR Controllers*

A major objective for the ac current regulators is to achieve zero phase and magnitude errors. Here, the synchronous reference frame equivalent PI (SRF-EPI) controller in the stationary frame was presented as an alternative solution for fundamental frequency reference tracking purposes [26], [28].

The synchronous reference frame equivalent integral controller is $F\angle\theta$, and $n<0$ refers to the signal is in negative sequence.

$$F=\begin{cases}\infty & n=1\\ \dfrac{2k_i}{\omega_0|n-1|} & n\neq 1\end{cases},\quad \theta=\begin{cases}0^\circ & n=1\\ -90^\circ & (n>1)\cup(n<0)\\ 90^\circ & 0<n<1\end{cases} \tag{1}$$

The proportional (*P*) controller in the *dq* synchronous frame is the same as the *P* controller in the *αβ* frame. Then, the SRF-EPI controller transfer function is:

$$G_{eq}(s)=k_P+F\angle\theta=k_P+F\cos\theta+jF\sin\theta \tag{2}$$

Compared with the SRF-EPI controller, the integral and

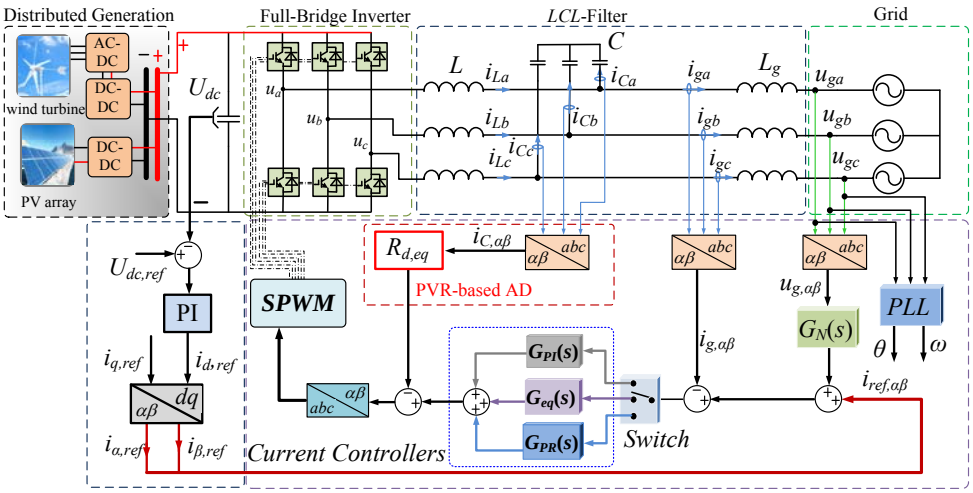


Fig. 1. System topology and control strategy of the three phase grid-connected inverters with *LCL* filter.

TABLE I
SYSTEM PARAMETERS OF THE LCL GRID-TIED INVERTER

| Symbol | Quantity | Value |
|---|---|---|
| $U_{dc}$ | Input voltage amplitude | 650 V |
| $u_g$ | Grid voltage | 311 V |
| $T_s$ | Sampling and switching period | 100 $\mu s$ |
| $\omega_0$ | Fundamental angular frequency | 100$\pi$ *rad/s* |
| $C$ | Capacitor | 10 $\mu$F |
| $L$ | Converter-side inductor | 1.8 *m*H |
| $L_g$ | Grid-side inductor | 1.8 *m*H |

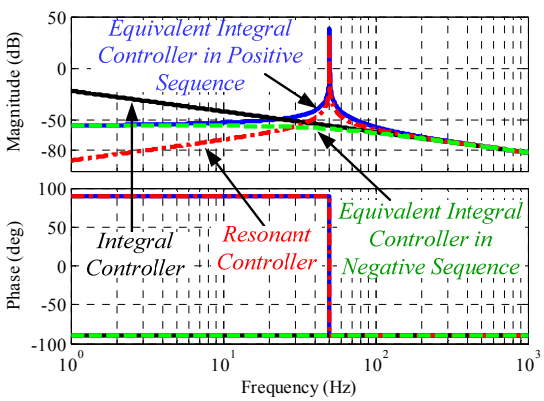


Fig. 2. Bode plots of the integral controller, resonant controller, and equivalent integrator controller in positive and negative sequences.

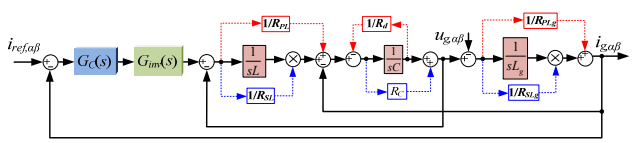

Fig. 3. Block diagram of various PD methods under grid current control for the three-phase inverter with *LCL* output filter.

resonant models of the PI and PR models are given by:

$$F_I = \begin{cases} \infty & n = 0 \\ \dfrac{k_i}{\omega_0 n} & n \neq 0 \end{cases}, \quad \theta_I = -90^\circ \tag{3}$$

$$F_R = \begin{cases} \infty & n = 1 \\ \dfrac{2k_i}{\omega_0^2(n^2+1)} & n \neq 1 \end{cases}, \quad \theta_R = \begin{cases} 0^\circ & n = 1 \\ -90^\circ & n > 1 \\ 90^\circ & n < 1 \end{cases} \tag{4}$$

The PI and PR current controllers are obtained by substituting (3) and (4) into (2), respectively.

Fig. 2 shows bode plots of the equivalent model $G_{eqI}$, and the resonant and integral controllers for the fundamental frequency signal tracking. It can be seen that the models show remarkable differences from each other in the low frequency range. Thus, direct implementation of the PR or PI models to predict system performance leads to inaccurate results. As for the phase characteristic, the equivalent PI controller $G_{eqI}$ in the positive sequence shows the same phase characteristic as the resonant model, while $G_{eqI}$ in the negative sequence shows the same phase-frequency characteristic as the integral model.

### *B. Passive Damping under Grid Current Feedback*

As shown in Fig. 3, the grid current is conventionally used as a feedback variable of the current controller to regulate the current injected into the grid. An amplitude peak exists at the resonant frequency of the LCL filter, which limits the design procedure of the current control-loop [6], [29].

A direct way to damp the LCL filter resonance is to insert a passive resistor in the inductor or capacitor of the *LCL* filter. In this case, the open-loop transfer functions of the grid current feedback control algorithm with various passive damping (PD) methods can be obtained as:

$$\begin{cases} G_{Series-L}(s) = \dfrac{G_C(s)G_{inv}(s)}{s^3LL_gC + s^2CL_gR_{SL} + s(L+L_g) + R_{SL}} \\ G_{Series-L_g}(s) = \dfrac{G_C(s)G_{inv}(s)}{s^3LL_gC + s^2CLR_{SL_g} + s(L+L_g) + R_{SL_g}} \end{cases} \tag{5}$$

$$\begin{cases} G_{Parallel-L}(s) = \dfrac{G_C(s)G_{inv}(s)(sL+R_{PL})}{s^3LL_gCR_{PL} + s^2LL_g + sR_{PL}(L+L_g)} \\ G_{Parallel-L_g}(s) = \dfrac{G_C(s)G_{inv}(s)(sL_g+R_{PL_g})}{s^3LL_gCR_{PL_g} + s^2LL_g + sR_{PL_g}(L+L_g)} \end{cases} \tag{6}$$

$$G_{Series-C}(s)=\frac{G_C(s)G_{inv}(s)(sCR_C+1)}{s^3LL_gC+s^2CR_C(L+L_g)+s(L+L_g)} \quad (7)$$

$$G_{Parallel-C}(s)=\frac{G_C(s)G_{inv}(s)R_d}{s^3LL_gCR_d+s^2LL_g+sR_d(L+L_g)} \quad (8)$$

where $G_{inv}(s)=U_{dc}/U_{tri}$ is the gain of the PWM inverter, $U_{dc}$ is the inverter dc voltage, and $U_{tri}=1$ is the carrier amplitude. $G_{Series-L}$ and $G_{Series-Lg}$ represent the open-loop transfer functions from $i_{ref,\alpha\beta}$ to $i_{g,\alpha\beta}$ when the damping resistor is connected in series with $L$ and $L_g$, respectively. $G_{Parallel-L}$ and $G_{Parallel-Lg}$ represent the open-loop transfer functions when the damping resistor is connected in parallel with $L$ and $L_g$, respectively. $G_{Series-C}$ and $G_{Parallel-C}$ are the open-loop transfer functions when the damping resistor is connected in series and in parallel with $C$, respectively.

Fig. 4 shows bode plots of the open-loop transfer functions with various PD schemes using the parameters in Table I when a PI current regulator is used. As shown in Fig. 4(a), an LCL filter with the PD methods has less attenuation in the low frequency (LF) region when a series resistor is connected with $L$ or $L_g$. As shown in Fig. 4(b), there is less attenuation in the high frequency (HF) region when a parallel resistor is connected with $L$ or $L_g$. As shown in Fig. 4(c), it can be seen that less attenuation is also caused when a series resistor is connected with $C$. As shown in Fig. 4(d), there is no impact on the LF and HF regions when a parallel resistor is connected with $C$. However, an excessive power loss always exists among the various PD schemes.

### *C. Virtual Resistance based Active Damping (AD) Strategy*

Compared with the PD methods, the active damping (AD) strategy is more flexible and more efficient. This method adopts a virtual resistor to eliminate power loss and can be easily incorporated into the existing control algorithm. The block diagram transformation of a traditional virtual resistor in series with a capacitor is derived in Fig. 5. However, it has been reported that the series virtual resistance based AD (SVR-based AD) needs to introduce differential element, that it causes noise amplification problems, and that the system can be unstable due to HF interference [17].

Therefore, an effective parallel virtual resistance based active damping (PVR-based AD) method in parallel with the capacitor for an LCL filter is proposed in this paper. This method avoids the LCL resonance problems, and satisfactory stability and robustness can be achieved. The principle diagram and the block diagram transformations of the PVR-based AD are shown in Fig. 6.

The transfer function of the PVR-based AD describing the grid current $i_{g,\alpha\beta}$ as a function of the voltage $u_{s,\alpha\beta}$ is given by:

$$G_{active-i_g u_s}(s)=\frac{i_{g,\alpha\beta}(s)}{u_{S,\alpha\beta}(s)}=\frac{1}{s(LL_gCs^2+R_{d,eq}L_gCs+(L+L_g))} \quad (9)$$

where $R_{d,eq}$ is the equivalent proportional term, $R_{d,eq}=L/(CR_d)$.

According to Fig. 6(b), the open-loop transfer function of

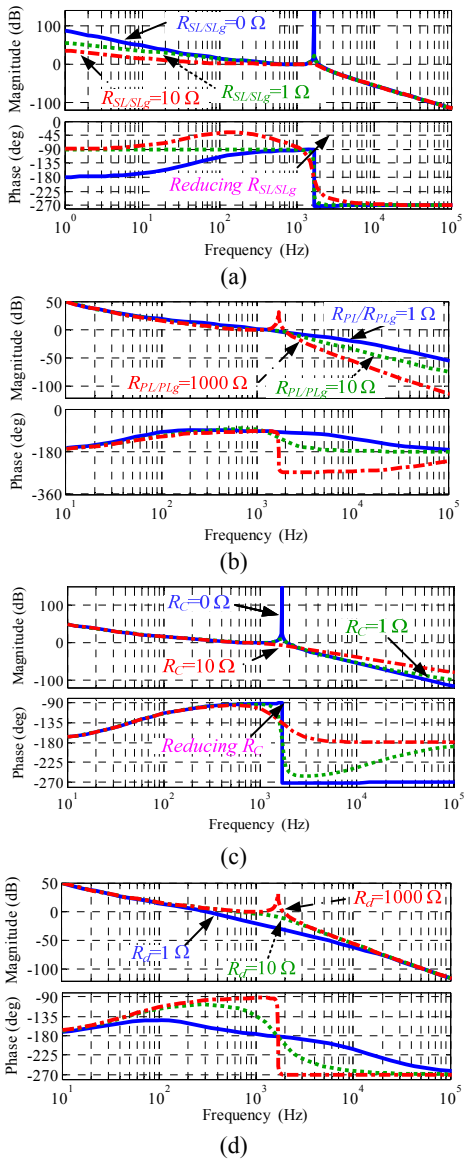


Fig. 4. Bode plots of the open-loop transfer function under grid current feedback control with various PD methods (Magnitude, phase are abbreviated as *Mag*, *Ph*): (a) The resistor in series with $L$ or $L_g$, (b) The resistor in parallel with $L$ or $L_g$, (c) The resistor in series with $C$, and (d) The resistor in parallel with $C$.

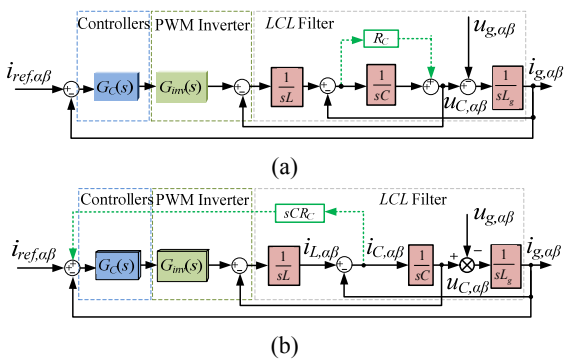


Fig. 5. Block diagram transformation of virtual resistor in series with capacitor: (a) Passive damping of capacitor series with resistor and (b) Equivalent SVR-based AD.

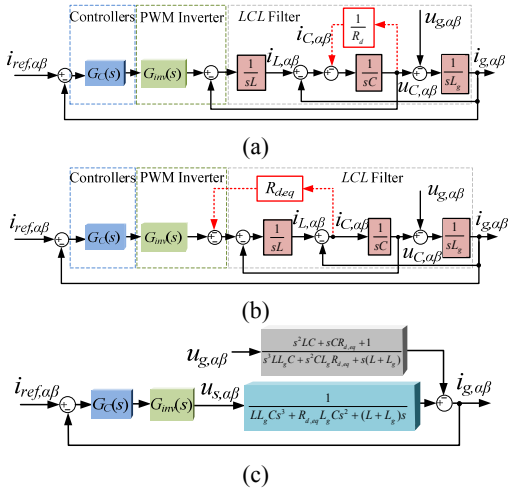


Fig. 6. Block diagram transformations of the PVR-based AD method: (a) PD scheme using parallel-connected resistor across capacitor, (b) Block transformation of PD control strategy in (a), and (c) The block diagram of parallel virtual resistance active damping.

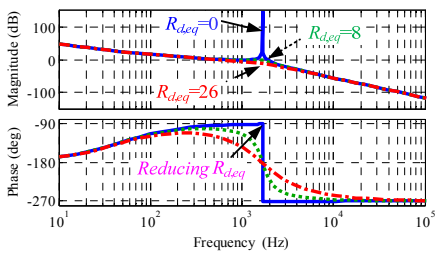


Fig. 7. Bode plots of the open-loop transfer function with PVR-based AD strategy.

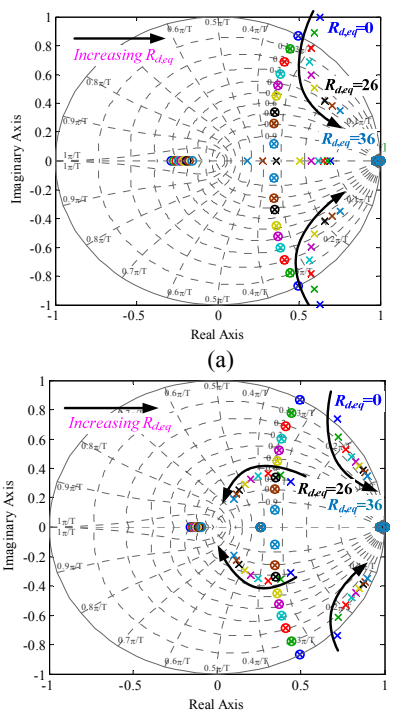


Fig. 8. Pole-zero map for close-loop transfer function with PVR-based AD strategy: (a) No delay and (b) $3/2T_s$ delay.

the PVR-based AD is given by:

$$G_{open}(s)=\frac{G_C(s)G_{inv}(s)}{LL_gCs^3+R_{d,eq}L_gCs^2+(L+L_g)s} \tag{10}$$

From (10), it can be seen that there are no unstable open-loop poles, i.e., $P$=0. If the PI current controller is used, using the parameters in Table I, the bode plots of the open-loop transfer function $G_{open}(s)$ with the AD method, when $R_{d,eq}$ is 0, 8 and 26, are illustrated in Fig. 7, respectively. The corresponding parallel virtual resistor $R_d$ is ∞, 22.5 Ω, and 6.9 Ω, respectively. According to the Nyquist stability criterion [7], the system is stable if $Q$=0.

$$Q=P+N_+-N_- \tag{11}$$

where $P$ is the number of unstable open-loop poles, and $N_+$ and $N_-$ are the number of times the path crosses the line in the clockwise and counter-clockwise directions. Hence, there is a one-to-one correspondence between the positive half of the Nyquist plot and the open-loop bode plot. $N_+$ and $N_-$ are two times the number of positive (from lower to upper) and negative (from upper to lower) crossings of $(2k+1)\pi$ ($k$ is an integer) in the open-loop bode plot in the frequency range with gains above 0 dB. For minimum phase system, i.e., where $P$=0, the system is stable if $N_+$=$N_-$ [29], [30].

1) When $R_{d,eq}$=0, the *PH-F* contour cross -180° from upper to lower at $f_{res}$ (in *Mag*>0 dB region). Thus, when $P$=0, $N_-$=0, $N_+$=2, and $Q$=2, the system is unstable.
2) When the feedback gain $R_{d,eq}$ increases, the *PH-F* contour cross -180° outside the *Mag*>0 dB region if the value of $R_{d,eq}$ is appropriate. Thus, when $P$=0, $N_-$=0, $N_+$=0, and $Q$=0, the system is stable. The cases for $R_{d,eq}$ =0, 8, 26 are shown in Fig. 8.

In order to intuitively show the variation tendency of the system stability when $R_{d,eq}$ varies, a discrete pole-zero map when the feedback gain $R_{d,eq}$ increases from 0 to 36 is illustrated in Fig. 8 by using the ZOH method. It can be seen that the system stability changes along with the delay time. The discrete open-loop transfer function of the current controller using the PVR-based AD scheme is:

$$G_{open}(z)=G_C(z)\times Z\left[G_d(s)G_{inv}(s)\frac{1-e^{-sT_s}}{s}\times\frac{1}{LL_gCs^3+R_{d,eq}L_gCs^2+(L+L_g)s}\right] \tag{12}$$

$$G_d(s)=e^{-sT_d} \tag{13}$$

where $G_d(s)$ represents the delay in the digital control, $T_d$ is the delay time which it is related to the analog-digital sampling process, the PWM generation process, and the hardware filtering [6], [26], [30]. The PWM switching frequency and the sampling frequency of the digital current controller are both selected to be 10 kHz.

Fig. 9 shows a frequency domain comparison between the PVR-based AD strategy, the PD method and the no damping scenario. It can be observed from Fig. 7 and Fig. 9 that the PVR-based AD method ensures effective damping

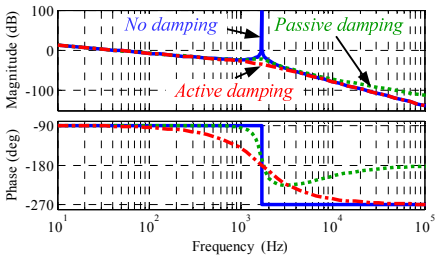


Fig. 9. Bode plots of PVR-based AD scheme compared with PD and no damping strategies.

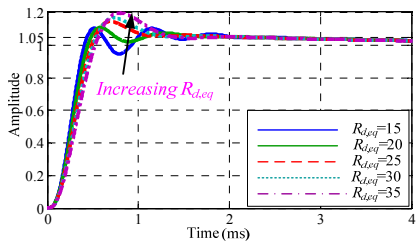


Fig. 10. Step response of the PVR-based AD scheme with different $R_{d,eq}$.

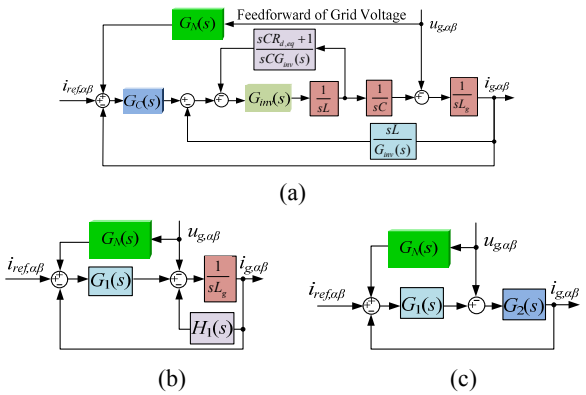


Fig. 11. Block diagram transformation of the PVR-based AD control algorithm with the grid voltage feed-forward loop.

characteristics. These figures also show that the attenuations in the LF and HF regions are not affected, which is an advantage over the other PD methods.

Once again referring to Fig. 8, it can be seen that values of $R_{d,eq}$ that are either too large or too small will affect the stability of the system. By gradually increasing $R_{d,eq}$, the poles can be moved close to the center of the unit circle. However, the poles will be moved away from the circle when $R_{d,eq}$ continues to increase. This has the effects of reducing the stability margin and increasing instability. Hence, it is necessary to optimize the damping coefficient $R_{d,eq}$, which ensures that the system has a sufficient stability margin and good dynamic performance.

Equation (9) is equivalent to a first order model combined with a second order plant model. In addition, the resonance is caused by the second order system. Notably, the resonance of the second order system is determined by the damping ratio $\xi$. The damping ratio $\xi$ in (9) is shown in (14). To eliminate the resonance, let $\xi$=0.707. Thus, the feedback gain is calculated as $R_{d,eq}$=26.8, i.e., the parallel virtual resistor $R_d$ is 6.7 Ω.

$$\xi = \frac{R_{d,eq}}{2L\omega_{res}} = \frac{R_{d,eq}}{2}\sqrt{\frac{L_g C}{(L+L_g)L}} \tag{14}$$

Fig. 10 shows the step responses of the PVR-based AD method with different $R_{d,eq}$ scenarios. It can be seen that the dynamic response is influenced by the value of $R_{d,eq}$. The overshoots as well as the oscillations are greatly reduced with an increasing $R_{d,eq}$ and the settling time is the shortest when $R_{d,eq}$=26.8. In summary, optimal performance is achieved when $R_{d,eq}$ equals 26.8, and it changes along with the delay time.

### *D. Grid Voltage Disturbance Rejection*

To mitigate the effect of grid voltage distortion on the quality of the output currents of the LCL-filter, the proportional resonant (PR) was introduced to provide infinite gain at the selected harmonic frequencies to guarantee sinusoidal grid currents [22], [31]. This method based is on the concept of harmonic impedance, which is to incorporate the grid voltage harmonics in the control loop through an additional feed-forward path to suppress the effects of unwanted harmonics. This does not affect the phase margin. However, the compensation accuracy of this approach is not satisfactory [32].

Block diagram transformations of the PVR-based AD algorithm with the grid voltage feed-forward loop are shown in Fig. 11. The current injected into the grid can be derived as:

$$\begin{aligned} i_{g,\alpha\beta}(s) &= \frac{W(s)}{1+W(s)} i_{ref,\alpha\beta}(s) - \frac{1-G_N(s)G_1(s)}{1+W(s)} G_2(s) u_{g,\alpha\beta}(s) \\ &= i_{g1}(s) + i_{g2}(s) \end{aligned} \tag{15}$$

where:

$$G_1(s) = \frac{G_C(s)G_{inv}(s)}{s^2LC + sCR_{d,eq} + 1} \tag{16}$$

$$G_2(s) = \frac{s^2LC + sCR_{d,eq} + 1}{s^3LL_gC + s^2CL_gR_{d,eq} + s(L+L_g)} \tag{17}$$

and $W(s)$=$G_1(s)G_2(s)$.

The transfer function from the grid voltage to the grid side current with the PVR-based AD is derived as:

$$\frac{i_{g,\alpha\beta}(s)}{u_{g,\alpha\beta}(s)} = \frac{s^2LC + sCR_{d,eq} + 1}{G_C(s)G_{inv}(s) + s^3LL_gC + s^2CL_gR_{d,eq} + s(L+L_g)} \tag{18}$$

Fig. 12 shows bode plots of (18) under no damping, and the PD and PVR-based AD cases without feed-forward of the grid voltage. It can be observed that a voltage disturbance near the resonance frequency results in large input currents in the no damping case. However, the PD and PVR-based AD schemes provide efficient resonance damping characteristics, and the PVR-based active damping scheme shows additional damping performance without causing additional power losses.

In order to mitigate the effect of the grid voltage on the

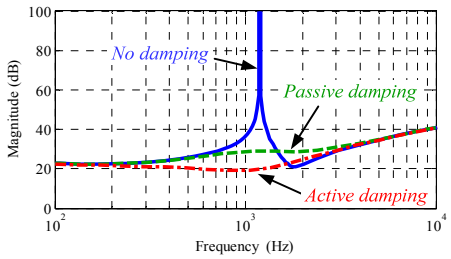


Fig. 12. Bode plots comparison of disturbance voltage to grid current of the harmonic admittance without the feed-forward of grid voltage.

quality of the LCL-filter currents, a feed-forward loop of the grid voltage and the multiple resonant regulators at the harmonic frequencies of the grid voltages are applied in the current loop. According to (15), setting 1-$G_N(s)G_1(s)$ to zero and adopting an approximate full compensation approach, the feed-forward function is derived as:

$$G_N(s)=\frac{1}{G_1(s)}=\frac{s^2LC+sCR_{d,eq}+1}{G_C(s)G_{inv}(s)} \tag{19}$$

Considering that derivative functions are difficult to implement and mainly for middle- and higher-frequency harmonics, and that the noise amplification problems reduce the stability margin, (19) is approximated by a first order low pass filter, and the higher order differential terms are neglected to avoid high frequency instabilities [29], [33]. As shown in Fig. 11(a), if the feed-forward control lies behind the current controller, the feed-forward factor has a very simple form, the proportional feed-forward is adopted, and $G_N(s)=1/G_{inv}(s)$. Moreover, multiple resonant controllers are achieved by paralleling several resonant blocks tuned to the harmonic frequencies to be compensated. This is expressed as:

$$G_h(s)=\sum_{h=5,7,11\ldots}\frac{2K_{ih}s}{s^2+(h\omega_0)^2} \tag{20}$$

where $h$ is the harmonic order to be compensated, $\omega_0$ represents the fundamental frequency, and $K_{ih}$ represents the respective resonant gain, which should be tuned relatively high, but within the stability limits, for minimizing the steady-state error. The dynamics of the fundamental PI, PR and SRF-EPI controllers in the stationary frame are unaffected when multiple resonant controllers are added, since the resonant controllers only compensate for frequencies that are very close to the selected resonant frequencies.

## III. Design Guidelines

### A. Stability of the SRF-EPI, PI and PR Controllers

The resonance damping and dynamic response have been taken into consideration for the aforementioned active damping design procedure. Thus, the current regulator $G_C(s)$ is designed to maintain suitable values for the PM, GM and cutoff frequency $f_c$. Generally, a PM in the range of 30°~60° and a GM≥3~6 dB are adopted for a compromise between the stability, dynamic response, and robustness [10], [14].

The cutoff frequency $f_c$ is typically kept lower than $f_s$, considering that the effect of attenuating the HF noise and $f_c$ generally can be chosen lower than 1/10 of $f_s$. Therefore, considering the frequency response of the system below the cutoff frequency, the influence of the capacitor of the LCL filter can be ignored and $G_{open}(s)$ can be approximated as:

$$G_{open}(s)\approx\frac{G_C(s)G_{inv}(s)}{(L+L_g)s} \tag{21}$$

Here, a PI controller is adopted to design the parameters for the PR and SRF-EPI controllers for comparison. At the cutoff frequency, the magnitude-frequency characteristic of the open-loop system is zero. As a result:

$$20\lg\left|G(j2\pi f_c)\right|\approx 20\lg\left|\frac{k_pG_{inv}(s)}{(L+L_g)*j2\pi f_c}\right|=0 \tag{22}$$

Thus, the controller gain $k_p$ is approximately represented as:

$$k_p\approx\frac{2\pi f_c(L+L_g)}{G_{inv}(s)} \tag{23}$$

which shows that $f_c$ is approximately proportional to $k_p$. Therefore, a larger $k_p$ means a faster dynamic response and a larger loop gain at low frequencies.

The steady-state error of $i_{g,\alpha\beta}$ at the fundamental frequency $\omega_0=2\pi f_0$ is an important index of the controller parameter design. As given by (15), assuming the adoption of the grid feed-forward control, the steady-state tracking error of the grid current $i_{g,\alpha\beta}$ can be calculated as:

$$E_g(s)=\frac{i_{g1}(s)-i_{ref}(s)}{i_{ref}(s)}=\frac{W(s)}{1+W(s)}-1 \tag{24}$$

The fundamental components of $i_{g2}$ and $u_{g,\alpha\beta}$ are denoted by $i_{g2}^*$ and $u_g^*$, respectively. Since the influence of the filter capacitor is negligible at the fundamental frequency $f_0$, considering (18), $i_{g2}^*$ can be approximated as:

$$i_{g2}^*\approx-\frac{u_g^*}{G_{inv}G_C(j2\pi f_0)} \tag{25}$$

Considering equation (21) and (25), $I_{g2}$ can be derived as:

$$I_{g2}\approx\frac{U_g}{G_{inv}\left|G_C(j2\pi f_0)\right|}\approx\frac{U_g}{2\pi f_0\left|G_{open2}(j2\pi f_0)\right|} \tag{26}$$

where $I_{g2}$ and $U_g$ are the root mean square (RMS) values of $i_{g2}^*$ and $u_g^*$, respectively.

According to (21) and the transfer function of the PI controller (26) can be rewritten as:

$$G_{open2}(f_0)=20\lg\left|G_{open2}(j2\pi f_0)\right|=20\lg\left|\frac{G_{inv}(k_p+\frac{k_i}{j2\pi f})}{j2\pi f_0(L+L_g)}\right| \tag{27}$$

Substituting (23) into (27), the integration gain is derived as:

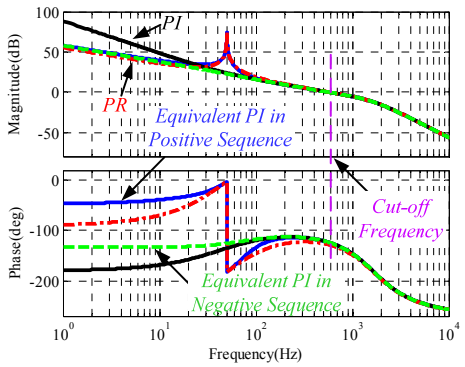


Fig. 13. Bode plots of the open-loop transfer function with PVR-based AD strategy.

$$k_i = \frac{4\pi^2 f_0 (L+L_g)}{G_{inv}} \sqrt{(10^{\frac{G_{open2}(f_0)}{20}} f_0)^2 - f_c^2} \tag{28}$$

According to (17) and (18), the PM of the system can be expressed as:

$$PM = 180^0 + \angle \frac{G_C(s)G_{inv}(s)}{LL_gCs^3 + R_{d,eq}L_gCs^2 + (L+L_g)s}\bigg|_{s=j2\pi f_C} \tag{29}$$

Substituting the transfer function of the PI into (29) yields:

$$PM = \arctan\frac{2\pi L(f_{res}^2 - f_c^2)}{G_{inv}f_c} - \arctan\frac{k_i}{2\pi f_c k_p} \tag{30}$$

Then, (30) can be rewritten as:

$$k_i = 2\pi f_C k_p \frac{2\pi L(f_{res}^2 - f_c^2) - G_{inv}f_C R_{d,eq}\tan PM}{2\pi L(f_{res}^2 - f_c^2)\tan PM + G_{inv}f_C R_{d,eq}} \tag{31}$$

Using the parameters of Table I, the resonance frequency $f_{res}$ of the *LCL* filter is equal to 1.68 kHz, and the value of the cutoff frequency $f_C$ is selected as 600Hz. In addition, the PM is selected as 50 degrees. With the system parameters given in Table I, the SRF-EPI, PI and PR controller parameters are selected as $k_p$=0.02 and $k_i$=5.77. Bode plots of the open-loop transfer function with the PVR-based AD, when $R_{d,eq}$ =26.8, is shown in Fig. 13. When the PI compensator is adopted, the GM and PM are 11.1 dB and 52.2 degrees, respectively. When an equivalent model of the synchronous-frame PI compensator in the stationary frame is adopted, the GM and PM are 11 dB and 44.9 degrees, respectively. When the PR compensator is adopted, the GM and PM are 9.56 dB and 31.5 degrees, respectively.

As shown in Fig. 13, except for the LF range, the open-loop bode plots of the stationary frame equivalent model of the PI controller in the positive sequence and the PR model are the same at the fundamental frequency, and are similar in the HF range. This indicates that the SRF-EPI controller in the stationary frame has similar performance to the PR controller in the stationary frame when tracking the fundamental frequency reference. Thus, the SRF-EPI controller has better performance than the PI and PR controllers at all frequencies when they are used in the stationary frame. Except for reference tracking at the fundamental frequency, the SRF-EPI controller in the stationary frame is not equivalent to the PI or PR controllers in the $\alpha\beta$ frame.

### *B. Impact of LCL-Parameter Variations*

Filter parameters drift away from the rated values due to the effects of parasitic parameters variations, operating conditions, temperature and grid impedance [10], [34]. To examine the robustness of a system with the PVR-based AD scheme of the SRF-EPI controller in the $\alpha\beta$ frame, bode plots of the compensated loop gain considering variations of the *LCL* filter parameters are given in Fig. 14. The grid impedance is considered to be a part of $L_g$. It is found that although $C$ varies from 7 to 13 $\mu$F (10 $\mu$F ± 30%), $L$ varies from 1.26 to 2.34 mH (1.8 mH ± 30%), or $L_g$ varies from 1.26 to 3.6 mH (1.8 mH -30% ~ +100%), the lowest cutoff frequency is still higher than 417 Hz, the PM is larger than 37.7 degrees, and the GM is larger than 9.84 dB. The frequency response characteristics in Fig.14 verify that the designed system has a strong robustness.

## IV. Simulation and Experimental Results

In order to verify the effectiveness of the proposed control strategies, simulation and experimental results of the proposed control strategy are presented and compared. The simulation studies were implemented using Matlab/Simulink. As shown in Fig. 15, an experimental setup was built and tested. The setup consists of two 2.2 kW Danfoss inverters, one working as a grid-connected inverter and the other controlled in the voltage control mode to emulate the grid with distortion. The dSPACE1006 platform was used to implement the control algorithms. In order to provide effective comparisons, all the control parameters are the same for the simulation and experiments. The system parameters are given in Table I and the SRF-EPI, PI and PR controller parameters are selected as $k_p$=0.02 and $k_i$=5.77.

Fig. 16 demonstrates the performance of the PVR-based AD strategy when the SRF-EPI controller is adopted. When the PVR-based AD strategy is enabled, the system is stable without resonance. However, when the active damping is disabled, resonance appears and the system becomes unstable. This shows that the PVR-based AD method is necessary for the SRF-EPI controller to maintain stability and to ensure harmonic-free grid currents.

Steady-state waveforms of the simulation and experimental results for the different controllers in the stationary frame with the proposed PVR-based AD method are shown in Fig. 17 and Fig. 21, respectively. As shown in Fig. 17, the fundamental RMS values of $i_{ga}$ (A phase) in Fig. 17(a), (b), and (c) are 1.63 A, 1.422 A, and 1.42A with a reference value of 1.414 A (RMS). The measured steady-state errors in Fig. 17(a), (b), and (c) are 15.3%, 0.57%, and 0.42% respectively.

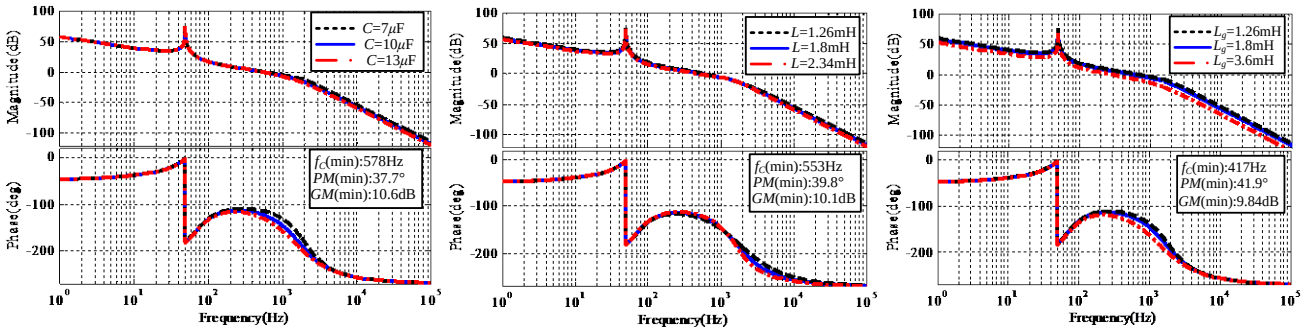


(a) (b) (c)

Fig. 14. Bode plots of the system considering the variations of the *LCL* filter parameters with PVR-based AD strategy: (a) $C$: 10 $\mu$F ± 30%, (b) $L$: 1.8 mH ± 30%, and (c) $L_g$: 1.8 mH -30% ~ +100%.

Fig. 15 Experimental setup.

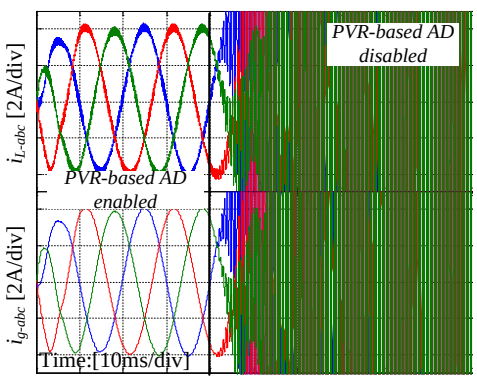


Fig. 16. Simulation result of the SRF-EPI control strategy when PVR-based AD strategy is disabled at 40ms.

In addition, the total harmonic distortions (THD) are 1.22%, 1.16%, and 1.12%, respectively. As shown in Fig. 21, the measured steady-state errors in Fig. 21(a), (b), and (c) are consistent with the simulation results. However, the current THDs are 1.28%, 4.8%, and 4.75%, respectively. It is noted that the THDs of the experimental results with the PR and SRF-EPI controllers are worse than that of the PI controller because the current of the PI controller has a higher amplitude due to the effect of steady state errors. Therefore, sufficient accuracy can be achieved by using the SRF-EPI controller, which is slightly better than the PR controller.

Simulation and experimental results of the transient responses when the reference steps up from 1.0 kW to 2.0 kW for the different controllers in the stationary frame with the PVR-based AD method are shown in Fig. 18 and Fig. 22, respectively. As shown in Fig. 18, good dynamic performances are achieved when the PR and SRF-EPI controllers in the $\alpha\beta$ frame are adopted. Fig. 22 shows that the transient response of the SRF-EPI controller is slightly better than that with the PR controller. The experimental results are consistent and in good agreement with the theoretical analysis and simulation results.

In order to evaluate the robustness of the SRF-EPI control scheme with the PVR-based AD method, simulation and experimental results under different virtual parallel damping resistance in the case of a control delay and the effect of grid voltage harmonics are presented.

Fig. 19 and Fig. 23 show the effects of the feedback gain $R_{d,eq}$ of the PVR-based AD method on the output current quality with a control delay time of $T_d$=1.5$T_s$, when $R_{d,eq}$ of the SRF-EPI controller is chosen to be 26.8, 18.8, and 6.8. The simulation and experimental results under different values of $R_{d,eq}$ with $T_d$=1.5$T_s$ are shown in Fig. 19 and Fig. 23.

Although the system is stable, the harmonic content increases dramatically when the value of $R_{d,eq}$ increases. In addition, the current THDs (phase A) in Fig. 19 (a), (b), and (c) are 35.82%, 6.04%, and 2.95%, respectively. The current THDs (phase A) of the experimental results in Fig. 23(a), (b), and (c) are 45%, 6.5%, and 3.6%, respectively.

Therefore, it is necessary to optimize the value of $R_{d,eq}$ to ensure a sufficient stability margin and a good dynamic response when a control delay is introduced.

To validate the performance of the control algorithm in the case of distorted grid conditions, the grid-emulator was distorted with 5th and 7th harmonics, with voltage THDs of 3% and 2%, respectively. Simulation and experimental results of the grid currents with the SRF-EPI controller in the stationary frame under different control scenarios are shown in Fig. 20 and Fig. 24. The multiple resonant controllers tuned at the 5th and 7th harmonics with $K_{ih}$=5 where $h$=5 and 7 are added to the SRF-EPI controller in the stationary frame with the proposed active damping method. The THDs of the simulated grid current $i_{ga}$ under different control scenarios are shown in

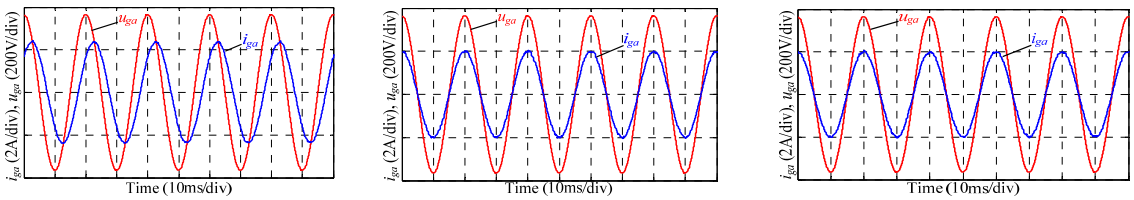


(a) (b) (c)

Fig. 17. Steady-state simulation results under 50% load condition with the proposed PVR-based AD strategy. (a) The PI controller. (b) The PR controller. (c) The SRF-EPI controller.

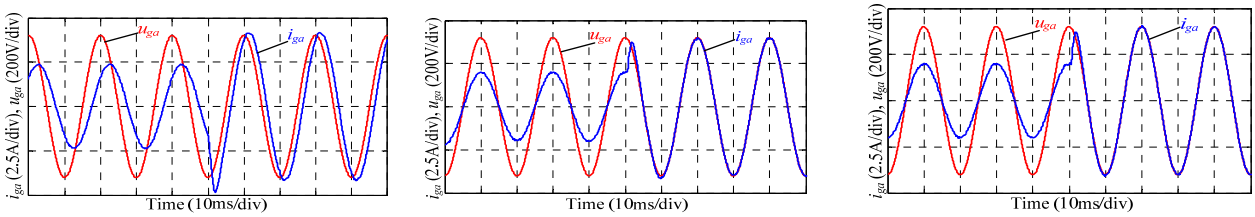


(a) (b) (c)

Fig. 18. Transient responses when the reference of $i_{ga}$ steps up from half-load to full-load with the proposed PVR-based AD strategy: (a) The PI controller, (b) The PR controller, and (c) The SRF-EPI controller.

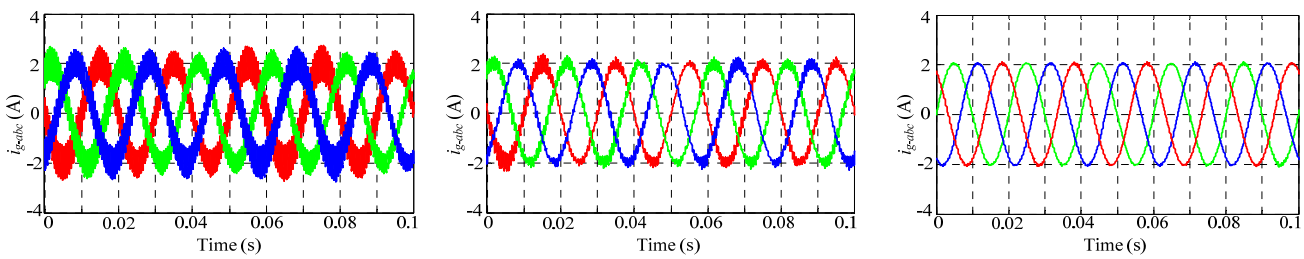


(a) (b) (c)

Fig. 19. Simulation results of different $R_{d,eq}$ with the delay time $T_d$=1.5$T_s$ when the SRF-EPI controller is used in the proposed PVR-based AD strategy: (a) $R_{d,eq}$ =26.8, (b) $R_{d,eq}$ =18.8, and (c) $R_{d,eq}$ =6.8.

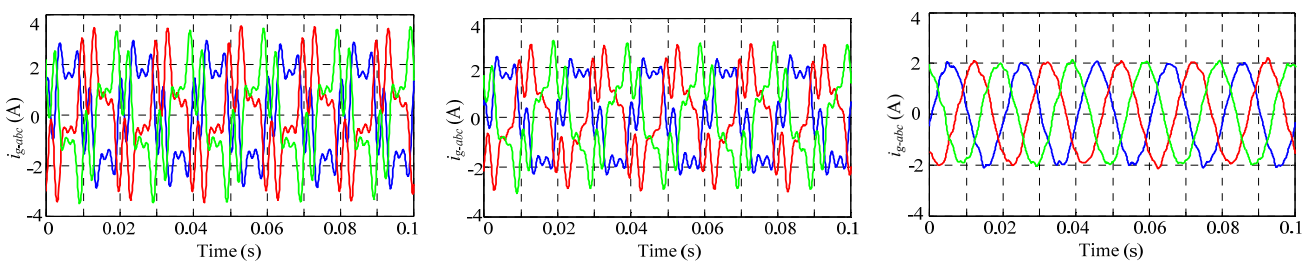


(a) (b) (c)

Fig. 20. Simulation results of the SRF-EPI controller with PVR-based AD strategy when grid voltages are highly distorted: (a) Without grid voltage feed-forward control, (b) With grid voltage feed-forward control, and (c) Combine with resonant controllers and grid voltage feed-forward control.

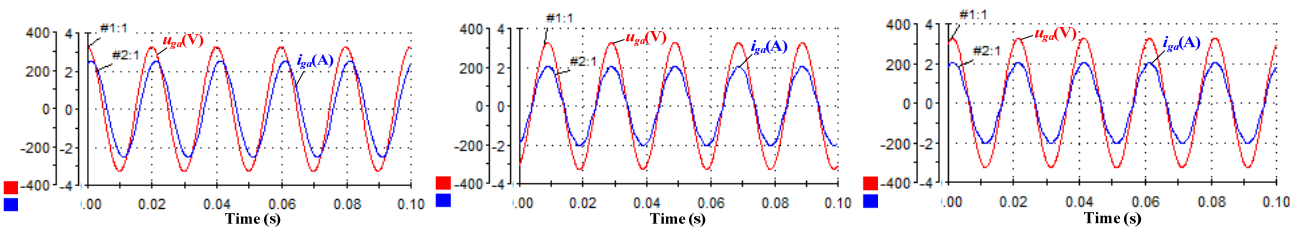


(a) (b) (c)

Fig. 21. Steady-state experimental results under half-load condition with the proposed PVR-based AD strategy: (a) The PI controller, (b) The PR controller, and (c) The SRF-EPI controller.

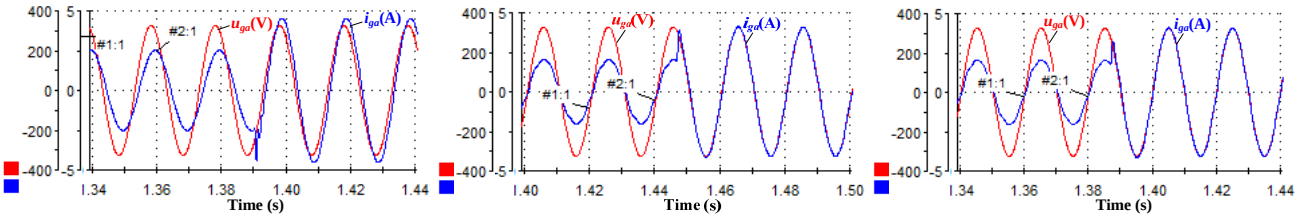


(a) (b) (c)

Fig. 22. Experimental transient waveforms when the reference of $i_{ga}$ steps from half load to full load with the proposed PVR-based AD strategy: (a) The PI controller, (b) The PR controller, and (c) The SRF-EPI controller.

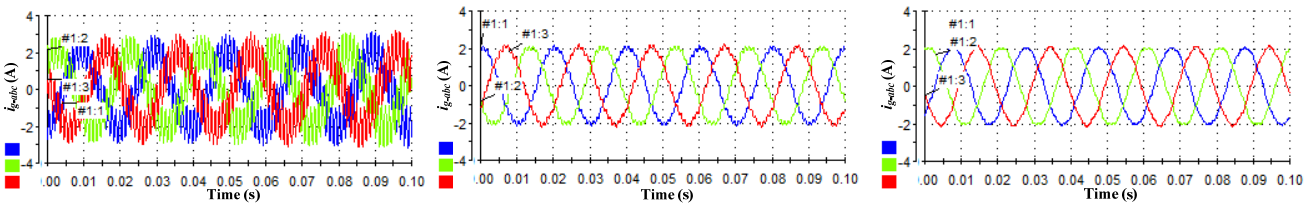


(a) (b) (c)

Fig. 23. Experimental results of different $R_{d,eq}$ with the delay time $T_d$=1.5$T_s$ when the SRF-EPI controller is used in the proposed PVR-based AD strategy: (a) $R_{d,eq}$ =26.8, (b) $R_{d,eq}$ =18.8, and (c) $R_{d,eq}$ =6.8.

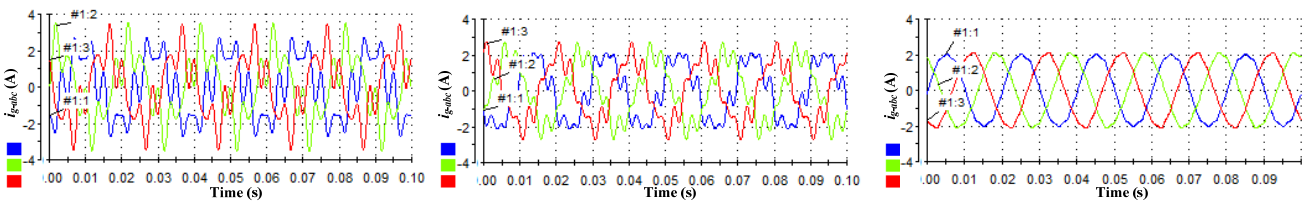


(a) (b) (c)

Fig. 24. Experimental results of the SRF-EPI controller in stationary frame with the PVR-based AD strategy when the grid voltages are highly distorted: (a) The SRF-EPI controller without grid voltage feed-forward control, (b) The SRF-EPI controller with grid voltage feed-forward control, and (c) The SRF-EPI controller combines with the resonant controllers and grid voltage feed-forward control.

Fig. 24, the current THDs of the experimental results are about 54.38%, 29.12% and 3.92%. This shows that when only the SRF-EPI controller is used, the grid currents are highly distorted due to harmonic distortion of the grid voltages. When the grid voltage feed-forward scheme is used in combination with the proposed control strategies, the current distortion can be effectively suppressed. However, the THD of the grid current is still high and the distortion in the grid currents cannot be rejected by the voltage feed-forward loop alone. However, when the SRF-EPI controller is adopted in combination with the grid voltage feed-forward loop and the multiple resonant controllers in the current loop, sinusoidal waveforms are guaranteed in the grid currents.

## V. Conclusion

In this paper, a stationary frame SRF-EPI control algorithm using the PVR-based AD method is proposed for three-phase *LCL* type grid-connected DG systems. It achieves a compromise between the resonance damping and the dynamic performance and makes it easier to stabilize the whole system. The accurate stationary frame of the SRF-EPI controller is introduced to achieve a high closed-loop bandwidth and good robustness. It is found that the SRF-EPI controller is equivalent to a PR controller in the stationary frame at the fundamental frequency. However, it shows different phase characteristics at other frequency ranges compared to the PR and PI controllers in the stationary frame.

In order to guarantee the quality of grid currents under non-ideal grid conditions, grid voltage feed-forward control with multiple resonant controllers in the harmonic frequencies is adopted, and the performance under the no damping, PD, and AD methods are compared. Furthermore, design guidelines of the systems of the SRF-EPI, PI and PR controllers are presented. Finally, simulation and experimental results of a three-phase *LCL*-based grid-connected inverter are presented to validate the proposed control approach.

## Acknowledgment

This work was supported by the National Natural Science Foundation of China (51307015), and the State Key Laboratory of Power Transmission Equipment & System Security and New Technology, Chongqing University (2007DA10512713405), and the Open Research Subject of

Sichuan Province Key Laboratory of Power Electronics Energy-Saving Technologies & Equipment (szjj2015-067), and by the Open Research Subject of Artificial Intelligence Key Laboratory of Sichuan Province (2015RZJ02).

## REFERENCES

[1] F. Blaabjerg, R. Teodorescu, M. Liserre, and A. Timbus, "Overview of control and grid synchronization for distributed power generation systems," *IEEE Trans. Ind. Electron.*, Vol. 53, No. 5, pp. 1398–1409, Oct. 2006.

[2] P. Sivakumar and M. S. Arutchelvi, "Enhanced controller topology for photovoltaic sourced grid connected inverters under unbalanced nonlinear loading," *Journal of Power Electronics*., Vol. 14, No. 2, pp. 369–382, Mar. 2014.

[3] L. Zhang, K. Sun, Y. Xing, and M. Xing, "H6 transformerless full-bridge PV grid-tied inverters," *IEEE Trans. Power Electron.*, Vol. 29, No. 3, pp. 1229-1238, Mar. 2014.

[4] L. Zhang, K. Sun, H. Hu, and Y. Xing, "A system-level control strategy of photovoltaic grid-tied generation systems for european efficiency enhancement," *IEEE Trans. Power Electron.*, Vol. 29, No. 7, pp. 3445-3453, Jul. 2014.

[5] J. He and Y. W. Li, "Generalized closed-loop control schemes with embedded virtual impedances for voltage source converters with LC or LCL filters," *IEEE Trans. Power Electron.*, Vol. 27, No. 4, pp. 1850–1861, Apr. 2012.

[6] S. Guoqiao, Z. Xuancai, Z. Jun, and X. Dehong, "A new feedback method for PR current control of LCL-filter-based grid-connected inverter," *IEEE Trans. Ind. Electron.*, Vol. 57, No. 6, pp. 2033–2041, Jun. 2010.

[7] J. Dannehl, M. Liserre, and F. W. Fuchs, "Filter-based active damping of voltage source converters with filter," *IEEE Trans. Ind. Electron.*, Vol. 58, No. 8, pp. 3623–3633, Aug. 2011.

[8] R. Pena-Alzola, M. Liserre, F. Blaabjerg, R. Sebastian, J. Dannehl, and F. W. Fuchs, "Analysis of the passive damping losses in LCL-filter-based grid converters," *IEEE Trans. Power Electron.*, Vol. 28, No. 6, pp. 2642–2646, Jun. 2013.

[9] R. Beres, X. Wang, F. Blaabjerg, C. L. Bak, and M. Liserre, "Comparative evaluation of passive damping topologies for parallel grid-connected converters with LCL filters," in *IEEE Power Electronics Conf.*, pp. 18-21, May 2014.

[10] J. Xu, S. Xie, and T. Tang, "Active damping-based control for grid-connected LCL-filtered inverter with injected grid current feedback only," *IEEE Trans. Ind. Electron.*, Vol. 61, No. 9, pp. 4746–4758, Sep. 2014.

[11] C. P. Dick, S. Richter, M. Rosekeit, J. Rolink, and R. W. De Doncker, "Active damping of LCL resonance with minimum sensor effort by means of a digital infinite impulse response filter," in *2007 European Conf. Power Electronics and Applications,* pp. 1–8, Sep. 2007.

[12] G. Shen, D. Xu, L. Cao, and X. Zhu, "An improved control strategy for grid-connected voltage source inverters with a LCL filter," *IEEE Trans. Power Electron.*, Vol. 23, No. 4, pp. 1899–1906, Jul. 2008.

[13] J. Dannehl, F. W. Fuchs, S. Hansen, and P. B. Thøgersen, "Investigation of active damping approaches for PI-based current control of grid-connected pulse width modulation converters with LCL filters," *IEEE Trans. Ind. Appl*., Vol. 46, No. 4, pp. 1509–1517, Jul./Aug. 2010.

[14] C. Bao, X. Ruan, X. Wang, W. Li, D. Pan, and K. Weng, "Step-by-step controller design for LCL-type grid-connected inverter with capacitor–current-feedback active-damping," *IEEE Trans. Power Electron.*, Vol. 29, No. 3, pp. 1239–1253, Mar. 2014.

[15] S. G. Parker, B. P. McGrath, and D. G. Holmes, "Regions of active damping control for LCL filters," *IEEE Trans. Ind. Appl*., Vol. 50, No. 1, pp. 424–432, Jan./Feb. 2014.

[16] M. Hanif, V. Khadkikar, W. Xiao, and J. L. Kirtley, "Two degrees of freedom active damping technique for filter-based grid connected PV systems," *IEEE Trans. Ind. Electron.*, Vol. 61, No. 6, pp. 2795–2803, Jun. 2014.

[17] Y. Lei, W. Xu, C. Mu, and Z. Zhao, "New hybrid damping strategy for grid-connected photovoltaic inverter with LCL filter," *IEEE Trans. Appl. Supercond.*, Vol. 24, No. 5, pp. 361–368, Oct. 2014.

[18] J. C. Vasquez, J. M. Guerrero, M. Savaghebi, J. Eloy-Garcia, and R. Teodorescu, "Modeling, analysis, and design of stationary-reference-frame droop-controlled parallel three-phase voltage source inverters," *IEEE Trans. Ind. Electron.*, Vol. 60, No. 4, pp. 1271–1280, Apr. 2013.

[19] N. He, D. Xu, Y. Zhu, J. Zhang, G. Shen, Y. Zhang, J. Ma, and C. Liu, "Weighted average current control in a three-phase grid inverter with an LCL filter," *IEEE Trans. Power Electron.*, Vol. 28, No. 6, pp. 2785–2797, Jun. 2013.

[20] X. Yuan, W. Merk, H. Stemmler, and J. Allmeling, "Stationary-frame generalized integrators for current control of active power filters with zero steady-state error for current harmonics of concern under unbalanced and distorted operating conditions," *IEEE Trans. Ind. Appl*., Vol. 38, No. 2, pp. 523–532, Mar./Apr. 2002.

[21] H. Yi, F. Zhuo, Y. Li, Y. Zhang, and W. Zhan, "Comparison analysis of resonant controllers for current regulation of selective active power filter with mixed current reference," *Journal of Power Electronics*., Vol. 13, No. 5, pp. 861–876, Sep. 2013.

[22] Y. Jia, J. Zhao, and X. Fu, "Direct grid current control of LCL filtered grid-connected inverter mitigating grid voltage disturbance," *IEEE Trans. Power Electron.*, Vol. 29, No. 3, pp. 1532–1541, Mar. 2014.

[23] M. A. Abusara, S. M. Sharkh, and P. Zanchetta, "Control of grid-connected inverters using adaptive repetitive and proportional resonant schemes," *Journal of Power Electronics*, Vol. 15, No. 2, pp. 518–529, Mar. 2015.

[24] X. Bao, F. Zhuo, Y. Tian, and P. Tan, "Simplified feedback linearization control of three-phase photovoltaic inverter with an LCL filter," *IEEE Trans. Power Electron.*, Vol. 28, No. 6, pp. 2739–2752, Jun. 2013.

[25] T. Yi, L. Poh Chiang, W. Peng, C. Fook Hoong, and G. Feng, "Exploring inherent damping characteristic of LCL-filters for three-phase grid-connected voltage source inverters," *IEEE Trans. Power Electron.*, Vol. 27, No. 3, pp. 1433–1443, Mar. 2012.

[26] C. Zou, Liu, S. Duan, and R. Li, "Stationary frame equivalent model of proportional-integral controller in *dq* synchronous frame," *IEEE Trans. Power Electron.*, Vol. 29, No. 9, pp. 4461–4465, Sep. 2014.

[27] G. Shen, X. Zhu, J. Zhang, and D. Xu, "A new feedback method for PR current control of LCL-filter-based grid-connected inverter," *IEEE Trans. Ind. Electron.*, Vol. 57, No. 6, pp. 2033–2041, Jun. 2010.

[28] D. N. Zmood and D. G. Holmes, "Stationary frame current regulation of PWM inverters with zero steady-state

error," *IEEE Trans. Power Electron.*, Vol. 18, No. 3, pp. 814–822, May. 2003.
[29] C. Zou, B. Liu, and R. Li, "Influence of delay on system stability and delay optimization of grid-connected inverters with LCL filter," *IEEE Trans. Ind. Inform.*, Vol. 10, No. 3, pp. 1775–1784, Aug. 2014.
[30] J. Xu, S. Xie, and T. Tang, "Evaluations of current control in weak grid case for grid-connected LCL-filtered inverter," *IET Power Electronics*, Vol. 6, No. 2, pp. 227–234, Feb. 2013.
[31] D. A. Timbus, M. Liserre, R. Teodorescu, P. Rodriguez, and F. Blaabjerg, "Evaluation of current controller for distributed power generation systems," *IEEE Trans. Power Electron.*, Vol. 24, No. 3, pp. 654–664, Mar. 2009.
[32] T. Abeyasekera, C. M. Johnson, D. J. Atkinson, and M. Armstrong, "Suppression of line voltage related distortion in current controlled grid connected inverters," *IEEE Trans. Power Electron.*, Vol. 20, No. 6, pp. 1393–1401, Nov. 2005.
[33] X. Wang, X. Ruan, S. Liu, and C. K. Tse, "Full feedforward of grid voltage for grid-connected inverter with LCL filter to suppress current distortion due to grid voltage harmonics," *IEEE Trans. Power Electron.*, Vol. 25, No. 12, pp. 3119–3127, Dec. 2010.
[34] K. Jalili and S. Bernet, "Design of LCL filters of active-front-end twolevel voltage-source converters," *IEEE Trans. Ind. Electron.*, Vol. 56, No. 5, pp. 1674–1689, May 2009.

**Yang Han** was born in Chengdu, China. He received his Ph.D. degree in Electrical Engineering from Shanghai Jiaotong University (SJTU), Shanghai, China, in 2010. He joined the Department of Power Electronics, School of Mechatronics Engineering, University of Electronic Science and Technology of China (UESTC), Chengdu, China, in 2010, and where he has been an Associate Professor since 2013. From March 2014 to March 2015, he was a Visiting Scholar in the Department of Energy Technology, Aalborg University, Aalborg, Denmark. His current research interests include ac/dc microgrids, power quality, grid-connected converters for renewable energy and DGs, active power filters, and static synchronous compensators (STATCOMs). He has authored more than 20 ISI-indexed journal papers in the areas of power electronics, power quality conditioners, and smart grids. He received Best Paper Awards from the 2013 Annual Conference of HVDC and Power Electronics Committee of the Chinese Society of Electrical Engineers (CSEE) in Chongqing, China, and the 4th International Conference on Power Quality in 2008 in Yangzhou, China.

**Pan Shen** was born in Hefei, China. He received his B.S. degree in Electrical Engineering and Automation from Anhui Agricultural University, Hefei, China, in 2013. He is presently working towards his M.S. degree in Power Electronics and Electric Drives at the University of Electronic Science and Technology of China (UESTC), Chengdu, China. His current research interests include power quality, power converters, ac/dc microgrids, power system automation, and active power filters.

**Josep M. Guerrero** received his B.S. degree in Telecommunications Engineering, his M.S. degree in Electronics Engineering, and his Ph.D. degree in Power Electronics from the Technical University of Catalonia, Barcelona, Spain, in 1997, 2000 and 2003, respectively. Since 2011, he has been a Full Professor in the Department of Energy Technology, Aalborg University, Aalborg, Denmark, where he is responsible for the Microgrid Research Program. Since 2012, he has been a guest Professor at the Chinese Academy of Science, Beijing, China, and the Nanjing University of Aeronautics and Astronautics, Nanjing, China; since 2014 he has been a Chair Professor at Shandong University, Shandong, China; and since 2015 he has been a distinguished guest Professor at Hunan University, Changsha, China. His current research interests include different microgrid aspects, including power electronics, distributed energy-storage systems, hierarchical and cooperative control, energy management systems, and the optimization of microgrids and islanded minigrids. He is an Associate Editor of the IEEE TRANSACTIONS ON POWER ELECTRONICS, the IEEE TRANSACTIONS ON INDUSTRIAL ELECTRONICS, and the IEEE Industrial Electronics Magazine. He is also an Editor of the IEEE TRANSACTIONS on SMART GRID and the IEEE TRANSACTIONS on ENERGY CONVERSION. He has been a Guest Editor of the IEEE TRANSACTIONS ON POWER ELECTRONICS Special Issues: Power Electronics for Wind Energy Conversion and Power Electronics for Microgrids; the IEEE TRANSACTIONS ON INDUSTRIAL ELECTRONICS Special Sections: Uninterruptible Power Supplies Systems, Renewable Energy Systems, Distributed Generation and Microgrids, and Industrial Applications and Implementation Issues of the Kalman Filter; and the IEEE TRANSACTIONS on SMART GRID Special Issue on Smart DC Distribution Systems. He was the Chair of the Renewable Energy Systems Technical Committee of the IEEE Industrial Electronics Society. In 2014, he was awarded by Thomson Reuters as Highly Cited Researcher, and in 2015 he was elevated to an IEEE Fellow for his contributions on 'distributed power systems and microgrids.'